Materials Advances

ROYAL SOCIETY OF CHEMISTRY

PAPER

View Article Online
View Journal | View Issue

Cite this: *Mater. Adv.*, 2025, **6**, 9528

Phosphate additive modification of C–S–H and C–A–S–H crystallization pathways

Yannick H. Emminger, Annika Bastian, Luca Ladner, Tobias Steiner and Cristina Ruiz-Agudo *

Phosphate-based additives are commonly used in concrete technology as hydration retarders and dispersion enhancers, playing a critical role in controlling cement hydration kinetics. This study examines how the molecular structure of three simple polyphosphate molecules affects the early formation of calcium silicate hydrate (C–S–H) and calcium aluminate silicate hydrate (C–A–S–H), the critical binding phases in modern cements that incorporate supplementary cementitious materials. We systematically compared two cyclic phosphate additives (phytic acid and hexametaphosphate) against one chain-like additive (tripolyphosphate), revealing structure-dependent effects on C–S–H and C–A–S–H formation. Our findings reveal that retardation occurs through dual pathways: calcium ion sequestration and formation of calcium–phosphate intermediate phases. The additives exhibit system-dependent behaviours—effectively retarding C–S–H formation while showing reduced retardation in C–A–S–H systems. The aluminium-containing system shows additional effects, with additives capable of stabilizing the C–A–S–H amorphous precursor phase. These distinct effects demonstrate that phosphate additives can produce multiple impacts beyond their intended retardation function depending on the composition of the cement. Understanding additive-hydrate interactions at the molecular level is therefore critical and may provide new avenues for controlling hydrate characteristics.

Received 15th July 2025,
Accepted 27th October 2025

DOI: 10.1039/d5ma00758e

rsc.li/materials-advances

1. Introduction

To optimize the properties of cementitious materials, retarders are added to adjust the setting time to meet the specific application requirements. Control over the setting is fundamental for diverse concrete applications across the construction industry. For instance, when fresh concrete requires extended workability periods—such as during long-distance transportation from batching plants to remote construction sites or vertical pumping operations in high-rise structures—carefully selected retarding admixtures maintain appropriate rheological properties throughout the required handling window. These retarding agents become particularly critical in elevated-temperature environments, where they effectively counterbalance the thermally induced acceleration of cement hydration that would otherwise yield premature setting, compromising proper placement and consolidation of the cementitious material.

The construction industry employs various chemical retarders that form complexes with calcium ions, including organic compounds such as carboxylic acids (tartaric,[1] gluconic,[2] and citric[3,4]), saccharides (sucrose and glucose),[5,6] lignosulfonates,[7] and organophosphonates,[8] as well as inorganic compounds where phosphate-based additives[9] and borates[10] are among the most used. The proposed mechanisms through which retarding agents influence cement hydration involve multiple molecular-level interactions that collectively delay the setting process.[11,12] Initially, these compounds undergo chemical adsorption onto cement particle surfaces, creating a protective layer that effectively reduces the dissolution rate of calcium silicate clinker phases. Most of the retarders also exhibit strong chelating properties, sequestering calcium ions from the pore solution and thereby maintaining ionic concentrations below the critical thresholds required for hydrate precipitation. This dual action—hindered dissolution and calcium complexation—works synergistically to inhibit the nucleation and early growth of essential binding phases, particularly calcium silicate hydrate (C–S–H) and portlandite ($Ca(OH)_2$).[11] Furthermore, certain retarders can form relatively insoluble calcium-additives phases that further contribute to the retardation effect by removing available calcium from the hydration process. This integrated action fundamentally alters the dissolution–precipitation equilibrium that governs the cement hydration process.[9]

Calcium silicate hydrate (C–S–H) and calcium aluminate silicate hydrate (C–A–S–H) represent the primary targets of retardation strategies, as their formation directly control

Physical Chemistry, University of Konstanz, Universitätsstrasse 10, 78457 Konstanz, Germany. E-mail: cristina.ruiz-agudo@uni-konstanz.de

cement setting and workability loss. These phases are primarily responsible for the mechanical strength[13] and durability[14] of cementitious systems, and their nucleation and subsequent growth govern the transition from plastic to rigid that defines the setting process. Recent studies have demonstrated that non-classical crystallization mechanisms[15]—where ion clusters or amorphous precursors aggregate before forming crystalline phases[16]—are also relevant for C–S–H and C–A–S–H.[17] Understanding how chemical additives such as retardants influence these formation pathways[18] is crucial for controlling the setting time and the workability retention in modern blended cements incorporating Al supplementary cementitious materials.

Among this diverse array of retarding admixtures, phosphate-based retarders have gained considerable interest due to their effective ability to delay cement hydration processes,[9] yet despite their widespread use, the molecular-level mechanisms by which they influence the nucleation and early growth of C–S–H and C–A–S–H binding phases remain poorly understood. This study aims to elucidate these specific mechanisms by investigating three exemplary phosphate-based additives with distinct structural configurations: phytic acid (organic cyclic), sodium hexametaphosphate (inorganic cyclic), and sodium tripolyphosphate (linear). We selected these P-compounds based on their known roles as retarders and dispersants in cementitious systems,[19–21] specifically choosing two cyclic phosphate compounds and one linear additive to systematically evaluating structure–function relationships. This comparative approach enables investigation of how different geometries—from organic cyclic to inorganic cyclic to linear arrangements—influence the hydrate formation process.

Phytic acid (Phy), an organic cyclic phosphate with six phosphate groups attached to an inositol ring, exhibits high binding affinity for calcium ions, enabling it to influence cement hydration and retard setting time.[19] Tests on the diametrical tensile strength of calcium silicate-based cement treated with phytic acid did not show any negative effects of the additive but left the strength unchanged.[22] Sodium hexametaphosphate (SHMP), an inorganic cyclic phosphate, is known to form calcium-chelating complexes[23] and is already used in the food industry as a chelator and deflocculator,[24] as well as a dispersing agent in cement pastes.[20] Tripolyphosphate (TriP), a linear phosphate additive, is a common hydration retarder[21] that complexes calcium ions[25] and can adsorb onto cement particles, leading to improved rheology through electrostatic repulsion.[26]

To elucidate the mechanisms of retardation, we employ a reproducible crystallization scenario[27] to clearly distinguish alterations in the early formation of these two critical binding phases. This study also aims to establish a reliable methodology for systematically comparing the effects of different additives on C–S–H and C–A–S–H nucleation and early growth, providing a standardized framework that can be extended to evaluate other chemical admixtures. Our multi-scale approach integrates *in situ* titration experiments with *ex situ* characterization techniques, including electron microscopy (TEM, SEM-EDX), Fourier Transform infrared spectroscopy (FTIR), and X-ray diffraction (XRD). Throughout the hydrate formation process, we monitor key solution parameters—including free-Ca^{2+} ion concentration, pH, transmittance, and conductivity—providing real-time insights into the reaction dynamics. The combination of these different probes enables precise identification of critical transition points such as nucleation events and phase transformations, revealing fundamental information about how additives modify these fundamental hydration processes.

2. Experimental

2.1. Reagents used

All reagents were employed without further purification. Sodium metasilicate nonahydrate ($Na_2SiO_3{\cdot}9H_2O$) was obtained from Acros Organics (CAS No. 13517-24-3). A 1 M calcium chloride ($CaCl_2$) solution, purchased from VWR Chemicals (CAS No. 10043-52-4), was diluted with Milli-Q purified water to achieve the desired concentration. Aluminium chloride hexahydrate ($AlCl_3{\cdot}6H_2O$) was sourced from Carl Roth GmbH & Co. KG (CAS No. 7784-13-6). Ethanol (pro analysis) was supplied by VWR Chemicals (CAS No. 64-17-5). The Phy is a 50 wt% solution in H_2O (CAS: 83-86-3) and was purchased together with sodium hexametaphosphate (CAS: 68915-31-1) from Sigma-Aldrich. Sodium tripolyphosphate (CAS: 7758-29-4) was provided by Auros Organics. A 1 M sodium hydroxide solution (CAS No. 1310-73-2) was purchased from Merck KGaA, Darmstadt, Germany. Transmission electron microscopy (TEM) grids were carbon support films on copper 400-mesh grids from Quantifoil® Micro Tools GmbH, Großlöbichau, Germany. Hydrophilic 0.22 μm PVDF membrane filters from Durapore® were used as filtration materials.

2.2. Synthesis of C–S–H and C–A–S–H in the presence of additives

C–S–H and C–A–S–H phases were synthesized using a double-titration system, described in detail elsewhere.[27] For C–S–H synthesis, 30 mL of a 40 mM $CaCl_2$ solution and 30 mL of a 40 mM Na_2SiO_3 solution were titrated concurrently at a rate of 0.1 mL min^{-1} into 100 mL of a solution containing additive concentrations of 10, 50, and 100 mg L^{-1}. These additive solutions were prepared by combining 1 mL, 5 mL, or 10 mL of a 1 g L^{-1} additive stock solution with 99 mL, 95 mL, or 90 mL of Milli-Q water, respectively, and adjusted to a pH of 12. For C–A–S–H synthesis, 8 mM $AlCl_3$ was incorporated into the $CaCl_2$ solution, with all other procedures identical to those used for C–S–H synthesis. Real-time conductivity, pH, transmittance, and calcium ion potential measurements were recorded throughout the experiments. Four replicates were prepared for each experimental condition. The resulting dispersions were filtered through 0.22 μm Durapore® membrane filters, washed with 300 mL of Milli-Q water, and dried in a vacuum chamber at 40 °C. After drying, the precipitates were stored in sealed glass containers for further *ex situ* analysis.

2.3. Aliquots-TEM-experiments

Separate titrations were conducted to facilitate transmission electron microscopy (TEM) analysis of intermediate stages during the formation of both C–S–H and C–A–S–H phases. At specified time intervals, 200 μL aliquots of the reaction mixture were extracted using a pipette and immediately quenched in 3 mL of ethanol. This ethanol-suspended solution was then drop-cast onto a TEM grid (carbon support films on Cu 400 mesh, Quantifoil Micro Tools GmbH) and allowed to air dry.

2.4. *Ex situ* analysis

2.4.1. Scanning electron microscopy (SEM). The morphology of the precipitates was primarily investigated through scanning electron microscopy (SEM) using a Zeiss Gemini 500 SEM (Carl Zeiss GmbH, Oberkochen, Germany). Samples were mounted on carbon tape and examined with a 3 kV electron beam without sputter coating, at a working distance of 5 mm. Elemental analysis was conducted *via* energy dispersive X-ray spectroscopy (EDX) within the same setup, using an acceleration voltage of 9 kV and a working distance of 8.5 mm. For each sample, 30 spectra were acquired from distinct locations, and the average elemental composition was subsequently calculated. Data processing was carried out using AZtec software (Oxford Instruments).

2.4.2. Fourier-transformed infrared (FTIR) spectroscopy. Fourier-transform infrared (FTIR) spectra were collected using a Cary 630 FTIR spectrometer (Agilent© Technologies Inc.) over a 600–4000 cm^{-1} spectral range. Measurements were conducted in transmittance mode, with 125 scans per step and a spectral resolution below 2 cm^{-1}. Data acquisition and processing were performed using Agilent's MicroLab software.

2.4.3. PXRD. Powder X-ray diffraction (PXRD) analyses were performed using a Bruker AXS D8 Advance diffractometer operating in Bragg–Brentano geometry. The instrument was equipped with an IμS X-ray source that produced Cu-K_α radiation with a wavelength of λ = 1.542 Å. Samples were scanned over a 2θ range from 2° to 70° in oscillating mode, with data acquisition managed by a LynxEye detector. The counting time was 4 s for increments of 0.02°. We calculated the full width at half maximum (FWHM) through Gaussian fitting using the Levenberg–Marquardt iteration algorithm.

3. Results & discussion

3.1. Time-resolved analysis of C–S–H formation

Real-time measurements of solution transmittance, calcium potential, conductivity, and pH were performed during the precipitation experiments to evaluate additive effects on calcium silicate hydrate (C–S–H) crystallization behaviour.

3.1.1. Transmittance. The transmittance measurements revealed significant modifications in the crystallization of C–S–H when the additives are present in the media (Fig. 1). In the additive-free reference experiment, the solution initially maintains high transmittance values (indicating optical clarity) until approximately 3300 s, when C–S–H nucleation begins (point of nucleation = PoN). From this point, transmittance decreases exponentially but does not reach zero values even after 5 hours of continuous reactant addition.[27] This baseline behaviour provides the reference against which we can evaluate the distinct impacts of the additives on C–S–H crystallization. All three investigated additives (Phy, SHMP, and TriP) induce a characteristic two-step process in the transmittance profiles, suggesting a fundamental modification of C–S–H formation compared to the reference system.

The transmittance data for Phy reveal a distinctive behaviour compared to the two other additives (Fig. 1a). Unlike the reference experiment, Phy induces an early and abrupt drop in transmittance, followed by a stable intermediate plateau persisting beyond the reference nucleation point. With increasing Phy concentration, three key changes become apparent in the transmittance curves (Fig. 1a): (1) the magnitude of the initial transmittance drop increases substantially; (2) the transition to the plateau phase occurs at progressively later time points; and (3) a substantial delay on the point of nucleation for C–S–H (marked by the second drop in the transmittance curve), with specific delays illustrated in Fig. 2.

At the first drop in the transmittance curve in the experiment with 100 mg L^{-1} Phy (1550 s), the Ca/Phy molar ratio reaches 5.79. This ratio appears critical for initiating the formation of calcium phytate precipitates, as evidenced by the sudden drop. In the experiments at 50 mg L^{-1}, the drop occurs earlier, around 800 s, when the Ca/Phy molar ratio reaches 5.86. The similarity between these two ratio values across the two concentrations suggests a consistent threshold

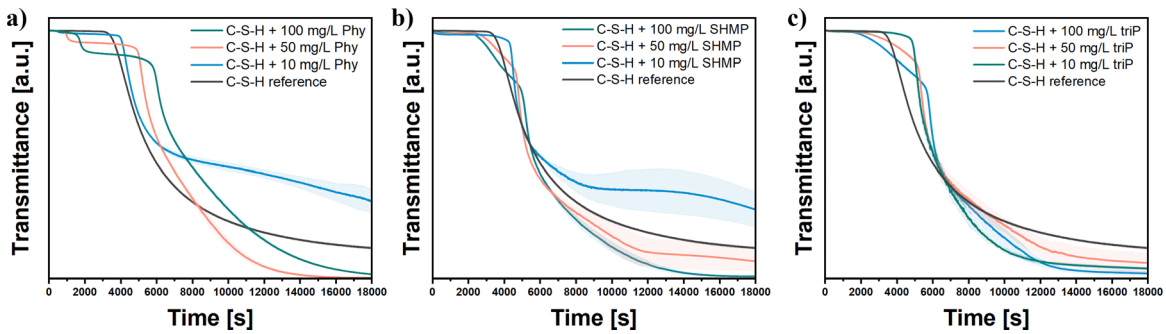

Fig. 1 *In situ* transmittance measurement data from the precipitation titration of C–S–H in presence of (a) phytic acid, (b) SHMP and (c) TriP in concentrations of 10, 50 and 100 mg L^{-1}.

interaction between calcium and Phy that triggers this initial precipitation event, independent of the absolute concentration of the additive. This observation aligns with the findings of Crea *et al.*, who demonstrated the formation of Ca-phytate phases with the compositions matching our determined values at pHs above 7.5.[28]

The subsequent plateau in the transmittance signal after the first drop indicates that the calcium phytate phase is stable, where particle size distribution and concentration most likely remain relatively constant. This metastable equilibrium persists until conditions favour the nucleation of C–S–H, marked by a second pronounced transmittance decrease followed by the characteristic exponential decay pattern observed in reference experiments.

Increasing concentrations of Phy produce a systematic delay in C–S–H nucleation, with the effect becoming more pronounced at higher dosages. Although the relationship between additive concentration and nucleation delay is not strictly linear, a clear qualitative trend emerges across the concentration range tested. Compared to the reference system, 600 s, 900 s, and 2200 s delays were observed with Phy concentrations of 10 mg L^{-1}, 50 mg L^{-1}, and 100 mg L^{-1}, respectively (Fig. 2). Calcium sequestration into the calcium-phytate phase likely accounts for a significant portion of this retardation effect, however, our results suggest that it cannot be the sole mechanism responsible for delaying C–S–H nucleation, as the observed delay exceeds what would be expected from simple calcium binding alone. In addition to the binding behaviour, a possible explanation could be a superimposed ion adsorption role on the clusters or nuclei and the resulting electrostatic repulsion against each other, which takes effect above a certain threshold.[9]

SHMP also seems to induce the formation of a Ca-additive phase, though with a seemingly different formation mechanism compared with Phy (Fig. 1b). Rather than the abrupt drop and stable plateau seen with Phy, SHMP produces a gradual, linear decrease in transmittance that progresses steadily until abruptly transitioning into the exponential decay pattern associated with C–S–H formation, marked by a distinct kink in the curve. The concentration-dependent behaviour of SHMP differs notably from that of Phy in several key aspects. While Phy shows delayed first transmittance drops at higher concentrations, SHMP exhibits the opposite trend - higher SHMP concentrations trigger an earlier first drop in transmittance. This inverse relationship is demonstrated across our tested concentrations (Fig. 2), with the first transmittance decrease occurring at approximately 3500 ± 200 s for 10 mg L^{-1}, 2300 ± 400 s for 50 mg L^{-1}, and 2300 ± 150 s for 100 mg L^{-1}. Like Phy, we attribute this initial decrease to the progressive formation of a calcium-SHMP phase, since EDX measurements (see below) confirm that Si content in the precipitates present at earlier times is much lower than P. However, the linear nature of the transmittance decline suggests a fundamentally different precipitation mechanism - rather than the sudden formation of a distinct intermediate phase observed with Phy, SHMP appears to induce a continuous growth of the precipitate formed in this first decrease of the transmittance.

Regarding C–S–H formation, the lowest concentration of SHMP (10 mg L^{-1}) already induces a significant delay in C–S–H nucleation compared to the reference system (Fig. 2). As SHMP concentration increases, the onset of C–S–H formation experiences a further non-linear delay that showed no concentration proportionality. Doubling the SHMP concentration from 50 to 100 mg L^{-1} produces a modest delay rather than the more significant extension observed with Phy. This behaviour contrasts notably with Phy, where concentration increases yield more predictable, proportional extensions of the induction period.

Poly-triphosphate (TriP) demonstrates behaviour remarkably like SHMP (Fig. 1c). The concentration-dependent trends

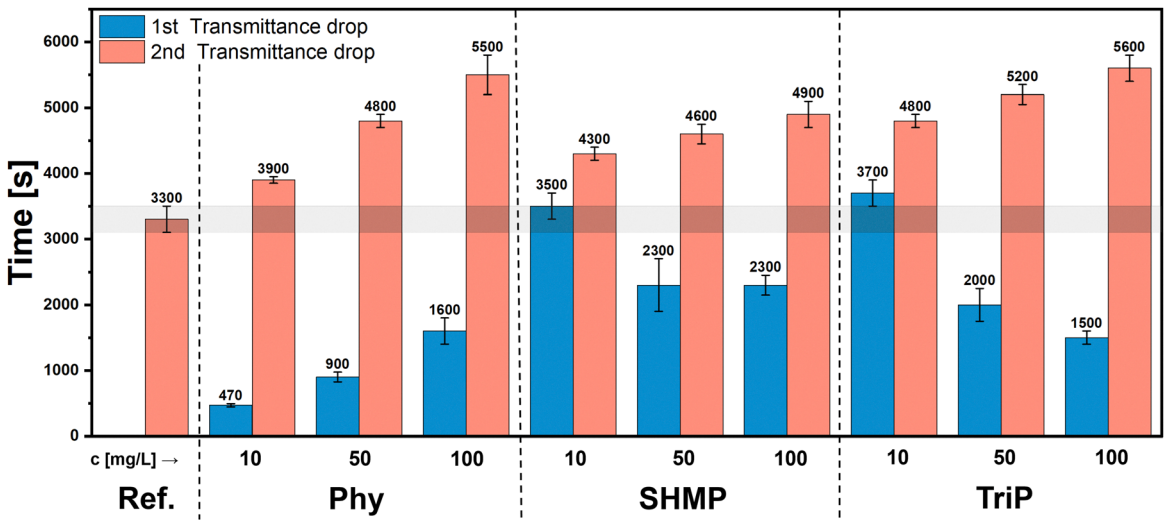

Fig. 2 Duration times until the first and second drop in transmittance was recorded during the precipitation titration of C–S–H in presence of the different additives at different concentrations.

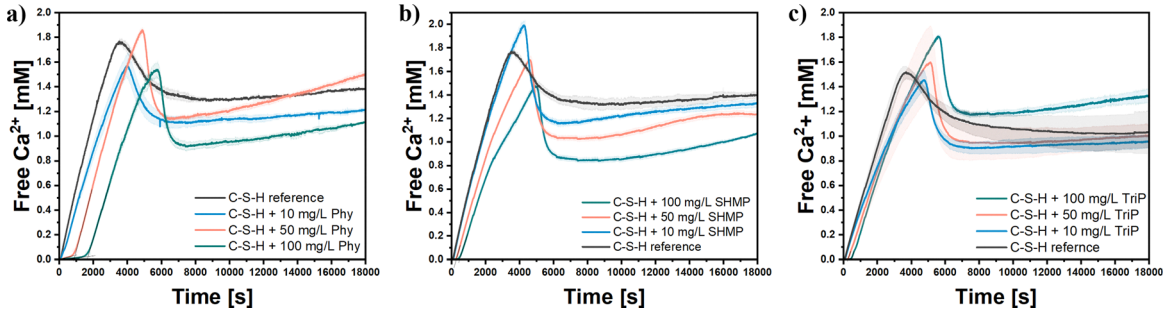

Fig. 3 *In situ* measurement data of the free-Ca^{2+} concentration during the precipitation titration experiments of C–S–H in presence of (a) phytic acid, (b) SHMP and (c) TriP at concentrations of 10, 50 and 100 mg L^{-1}.

mirror those observed with SHMP - higher concentrations of TriP produce earlier formation of the transition state, with the first transmittance decrease occurring sooner as additive concentration increases. Additionally, higher TriP concentrations generate steeper negative slopes in the transmittance curves during this intermediate stage, suggesting an acceleration of its formation process with increasing additive levels (Fig. 2). C–S–H formation is also delayed by TriP, following the general pattern observed with the SHMP. Notably, even the lowest concentration tested (10 mg L^{-1}) produced a substantial delay in C–S–H nucleation, indicating TriP's high efficiency as a retardation agent even at minimal dosages.

3.1.2. Free-Ca^{2+} concentration. In the reference experiment, free Ca^{2+} concentration exhibits a linear increase with continuous addition of reactants until reaching a maximum, after which, calcium is heavily consumed and the free Ca^{2+} decreases. This point correlates with the main drop in the transmittance curve, signifying C–S–H nucleation.

Experiments incorporating additives reveal additional crystallization stages (Fig. 3), only detectable in the calcium potential measurements and not in transmittance data, thereby providing complementary insights. Each additive initially establishes a distinctive calcium-binding regime wherein free Ca^{2+} concentrations remain negligible despite continuous calcium addition to the solution (Fig. S1). The calcium-binding demonstrates clear concentration dependence across all three additives, with higher additive concentrations predictably extending the duration of the calcium sequestration period. From our data, we quantified the calcium-binding capacity for each additive. Analysing the 100 mg L^{-1} and 50 mg L^{-1} experimental conditions, our calculations reveal the average Ca/P ratio at the end of each additive's calcium sequestration period to be 0.971 ± 0.090 for Phy, 0.201 ± 0.001 for SHMP, and 0.269 ± 0.015 for TriP.

Due to fundamental differences in their molecular structures, Phy demonstrates superior calcium-binding capacity per phosphorus atom compared to SHMP. Phy contains R–O–PO_3^{2-}groups, where each phosphate moiety carries two negative charges, enabling each phosphate group to bind one calcium ion. This arrangement theoretically allows Phy to bind up to 6 Ca^{2+} ions per molecule with its 6 phosphate groups, yielding an optimal binding ratio of 1, which aligns well with the measured one (0.971 ± 0.090).

Although SHMP has an equivalent number of phosphate groups arranged in a cyclic structure, the linking between each phosphate (–O–PO_2^-–O–) produces only one negative charge per moiety. Consequently, a SHMP molecule can theoretically bind a maximum of 3 Ca^{2+} ions, resulting in a P binding ratio of 0.5—half the calcium-binding efficiency of Phy. The measured value for SHMP (0.21 ± 0.01) is lower than theoretical predictions, likely due to its instability at high pH values. Furthermore, too precise statements cannot be made since the additive material used has varying molecular weights. TriP binding is determined by two terminal –O–PO_3^{2-} groups, each capable of binding one calcium ion, complemented by a middle group carrying one negative charge. This arrangement theoretically enables TriP to bind approximately 2.5 Ca^{2+} ions per molecule, giving a theoretical calcium-binding efficiency per phosphate group (Ca/P = 0.833) that positions it between Phy and SHMP. However, our experimental measurements revealed a significantly lower Ca/P ratio of 0.27 ± 0.04. TriP however, like SHMP, is a complex mixture with varying molecular weights, which subjects the calculated determination to errors.

Despite the fundamental structural differences between TriP (linear chain configuration) and SHMP (cyclic arrangement) at neutral pH, both additives exhibited similar Ca/P ratios under experimental conditions. While Phy most likely maintains its structural integrity due to the stable inositol ring backbone, the phosphate–oxygen–phosphate bonds in SHMP and TriP are vulnerable to nucleophilic attack by hydroxide ions.[29] ^{31}P-NMR studies have demonstrated that condensed phosphate additives undergo hydrolysis to form ortho and pyrophosphate species in similar cementitious systems.[30] This hydrolysis in highly alkaline cement pore solutions[31–33] likely accounts for their reduced calcium-binding capacities compared to theoretical predictions.

Following the exhaustion of their calcium-binding capacity by complexation, a secondary regime emerges characterized by linear increases in free Ca^{2+} for all three additives (Fig. 3). This increase exhibits a less steep slope compared to the reference experiment, providing evidence that these additives continue to interact with calcium ions beyond their initial complexation phase, perhaps interacting as well with more complex prenucleation species. In the case of Phy (Fig. 3a), this linear regime persists without significant deviation, suggesting a consistent secondary interaction mechanism after the binding phase until

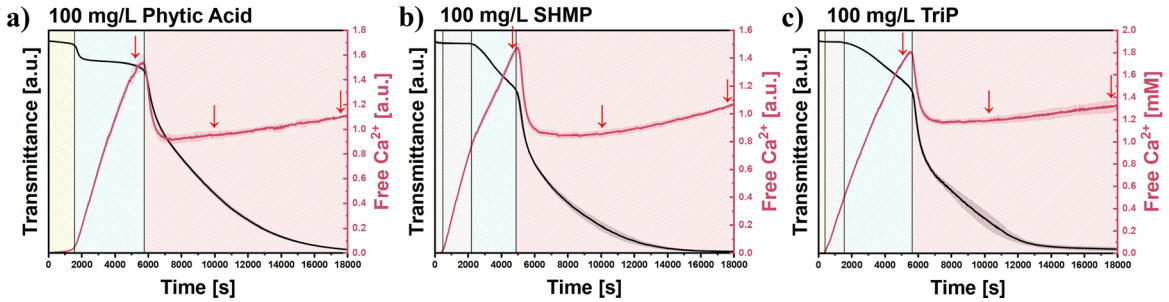

Fig. 4 Different regimes of the nucleation and crystallization of C–S–H in presence of (a) phytic acid, (b) SHMP and (c) TriP at concentrations of 100 mg L^{-1}, shown by the transmittance and Free-Ca^{2+} data.

C–S–H nucleation occurs. Calcium binding calculations suggest almost complete additive consumption due to the formation of the Ca-phytate phase, with potentially no free phytate remaining in solution. However, for both SHMP (Fig. 3b) and TriP (Fig. 3c), a distinctive inflection point (kink) appears in the calcium concentration curve, after which the slope is reduced. This kink indicates that these additives transition to another interaction with calcium ions.

At later experimental stages, the free-Ca^{2+} concentration eventually reaches its maximum value for all three additives before decreasing steadily, mirroring the characteristic pattern observed in reference experiments. This calcium depletion phase coincides precisely with the previously characterized second and more pronounced drop in the transmittance signal. The temporal synchronization of these two independent measurements—decreasing calcium concentration and diminishing light transmission—provides evidence that substantial calcium consumption occurs, corresponding to the nucleation and growth of C–S–H.

3.1.3. Crystallization regimes. The simultaneous analysis of transmittance and free-Ca^{2+} data exposes distinct stages in C–S–H crystallization in the presence of the phosphate-based additives (Fig. 4 and Fig. S2) that would be overlooked when examining either measurement alone. During the initial calcium-binding phase, the solution maintains clarity (high transmittance) for all additives similar to the reference (Fig. S3a), indicating the formation of soluble complexes that do not alter light scattering. Following this binding phase, each additive triggers distinctly different solution behaviours.

For Phy (Fig. 4a), transmittance sharply decreases soon after the Ca-binding regime concludes, establishing a persistent plateau that extends until C–S–H nucleation. Throughout this plateau phase, free-Ca^{2+} concentration rises steadily until reaching its maximum at the onset of C–S–H nucleation. This coupling between the end of the Ca-binding regime and the abrupt change in the solution's optical properties suggests that the solution undergoes a rapid transformation process, most likely the nucleation of the calcium-phytate phase, which would significantly alter light-scattering properties without consuming additional calcium ions.

A different process is observed for SHMP (Fig. 4b) and TriP (Fig. 4c). After the calcium-binding phase concludes, the solution typically maintains its clarity while free-Ca^{2+} increases linearly, suggesting the coexistence of various solute species such as Ca–P complexes, free-Ca^{2+} ions, and potentially other calcium-based species in solution, though their exact nature and distribution remain uncertain. Subsequently, the first decrease in transmittance coincides with a distinct inflection in the calcium concentration curve. This synchronization is especially evident in SHMP experiments (Fig. 4b), where both measurements align precisely, indicates the formation of light-scattering entities that steadily bind calcium. Despite their structural differences, these coordinated changes in optical properties and calcium dynamics suggest that SHMP and TriP form comparable entities during this intermediate regime. As titration curves alone cannot reveal the exact nature of these entities, complementary *ex situ* TEM and EDX analysis were conducted to get deeper insights into these intermediate phases.

Finally, at later stages, the second pronounced drop in transmittance coincides perfectly with the maximum in the free-calcium curve, signalling the extensive formation of C–S–H throughout the system.

3.1.4. Analysis of intermediate phases during C–S–H formation. To elucidate the evolution of intermediate phases during C–S–H crystallization, aliquots from reaction media containing the three additives (100 mg L^{-1}) were extracted at strategic time points (Fig. 4) and analysed by TEM and SEM (Fig. 5). Samples were collected at transition states between characteristic transmittance drops (5000 s and 1000 s) for each additive system and after the completion of reactant addition (18 000 s). Reference images are shown in Fig. S4.

With Phy, the TEM analysis of the first aliquot showed discrete and small globules (Fig. 5a), agreeing with the stable plateau in the transmittance curve. Quantitative EDX analysis (Fig. 6) yielded an average Ca/P ratio of 2.25 ± 0.40; notably, silicon was also detected in these early precipitates. The abrupt drop in transmittance and the lack of inflection points in the free-Ca^{2+} curve support a mechanism of rapid, stoichiometric precipitation of insoluble calcium phytate particles[34] once a critical Ca/phytate ratio is reached.[28] The Ca/P ratio in the solids, which exceeds the stoichiometric value expected for a pure calcium phytate phase, and the concurrent presence of silicon suggest the presence at that early time of an

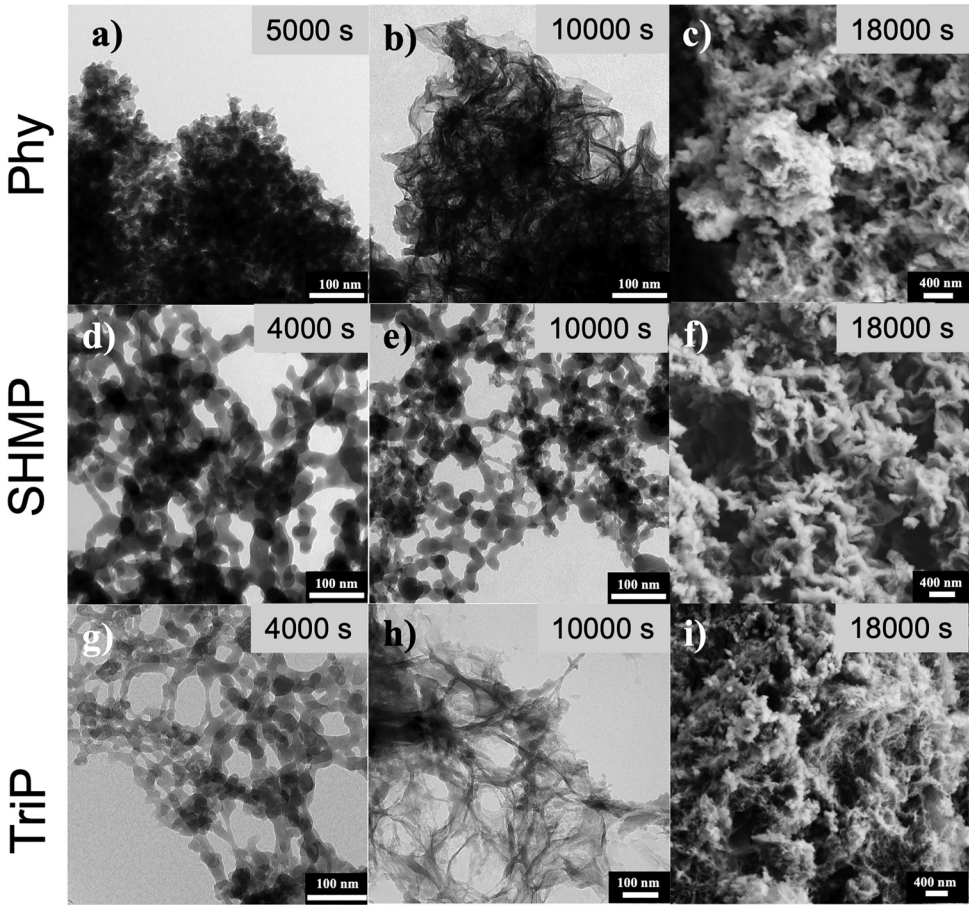

Fig. 5 TEM (a–h) and SEM (c, f and i) images of the various aliquots taken at different time spots during the precipitation titration in presence of phytic acid (a–c), SHMP (d–f) and TriP (g–i).

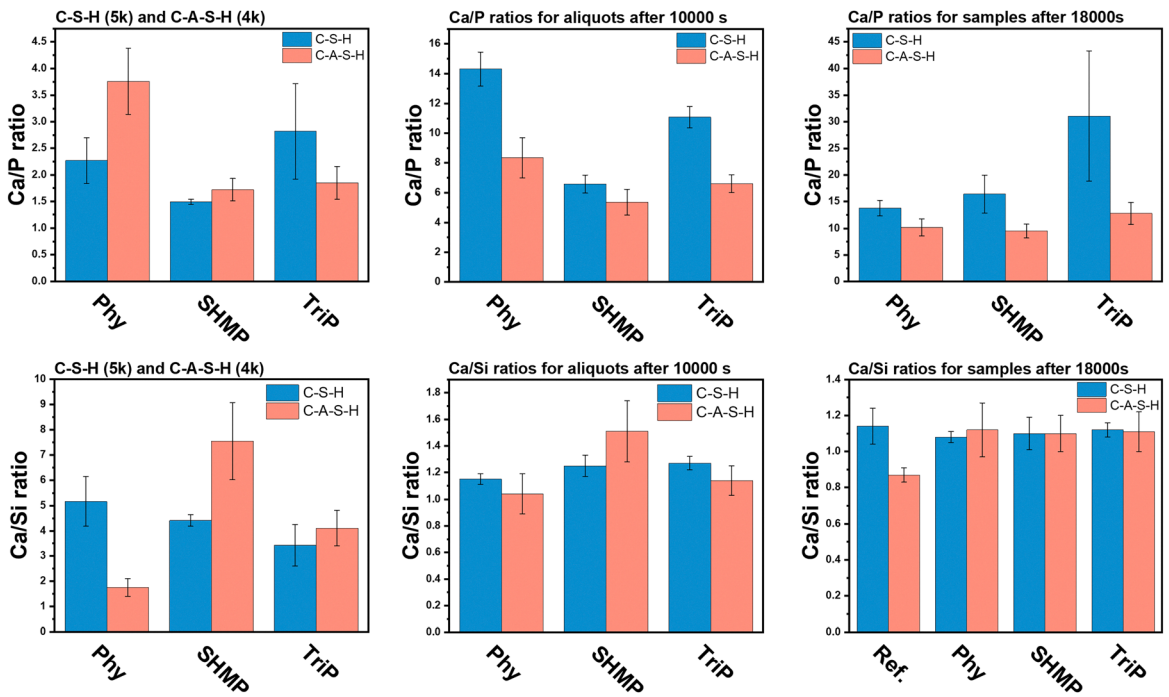

Fig. 6 Elemental compositions obtained by quantitative EDX analysis. Shown are the Ca/P ratios as well as the Ca/Si ratios of all aliquots of C–S–H and C–A–S–H.

additional Ca–Si-bearing phase(s) during these initial stages of precipitation.

By 10 000 s, C–S–H sheets had become the primary precipitated phase (Fig. 5b), which remained the predominant morphology at 18 000 s (Fig. 5c). Compositional analysis revealed a substantial reduction in the Ca/Si atomic ratio across the three aliquots (Fig. 6b–d), approaching values near 1.0, characteristic of the reference C–S–H. Concurrently, phosphorus content diminished significantly, marking the transition from initial calcium phosphate-rich precipitates at early ages to the establishment of a C–S–H-dominated material upon the second drop in the transmittance. Notably, the phosphorus content in the 18 000 s samples approached the theoretical maximum of 1.75 wt% phosphate in the final material. This theoretical value was calculated based on the stoichiometry of Ca-phytate precipitation, the initial additive concentration, and an estimation of C–S–H formation derived from measured free-Ca^{2+} concentration in solution. The close agreement between experimental and theoretical values indicates that Ca-phytate salts remained largely undissolved during the experimental period, a behaviour is consistent with the characteristically low solubility of phytate salts.[34]

In contrast, the SHMP and TriP systems exhibited markedly different early-phase morphologies compared with Phy. TEM analyses at 5000 s revealed ill-defined, interconnected globular assemblies (Fig. 5d and g) and bridging networks, consistent with the formation of calcium–phosphate coacervates *via* liquid–liquid phase separation.[28] These morphologies, characterized by dense regions with thin bridges and evolving three-dimensional networks, align with the gradual, linear decrease in transmittance (Fig. 1b and c) and the distinct inflection points in the free-Ca^{2+} concentration curves (Fig. 3b and c), both indicative of progressive coacervate phase development as Ca^{2+} binding increases in solution.[35,36] The coacervation process is driven by electrostatic interactions between anionic phosphate groups and Ca^{2+} ions, resulting in charge neutralization, reduced repulsion, and eventual chain association—a characteristic mechanism of polyelectrolyte-driven phase separation.[37] This sequence yields a dense, calcium/phosphate-rich coacervate phase (Fig. 6a), as confirmed by EDX (Ca/P ratios of 1.50 ± 0.05 for SHMP and 2.80 ± 0.90 for TriP), with significant silicon incorporation also detected.

These interconnected assemblies persisted for 10 000 s in the case of the SHMP (Fig. 5e). Still, the samples underwent compositional evolution, as evidenced by the reduced Ca/Si ratio (Fig. 6). This reduction likely reflects the progressive formation of C–S–H phases. In the case of TriP, after 10 000 s the sample evolved into thin (5–20 nm) neuronal-like structures (Fig. 5h and Fig. 7a and b) in which Ca and Si were the predominant elements (Fig. 7c and d) and P was detected as a minor component within the network (Fig. 7). This morphological development could be attributed to C–S–H formation utilizing the coacervate as a heterogeneous nucleation site, with its growth potentially proceeding outward from this organic template.

As the reaction progresses, at 18 000 s, the morphological transition from the coacervate networks to well-developed C–S–H sheets (Fig. 5f and i) becomes increasingly evident, accompanied by a substantial decrease in Ca/Si ratios (Fig. 6), ultimately converging to the characteristic C–S–H composition and coral-like, porous superstructure observed in the reference system. Compositional changes between the 10 000 s and 18 000 s samples for all additives are considerably less pronounced, most likely due to the progressive dilution of Ca–phosphate phases as C–S–H formation proceeds. Regarding the fate of the coacervate phases —whether they undergo structural transformation, gradual dissolution, or remain stable—direct experimental evidence is limited, and definitive conclusions

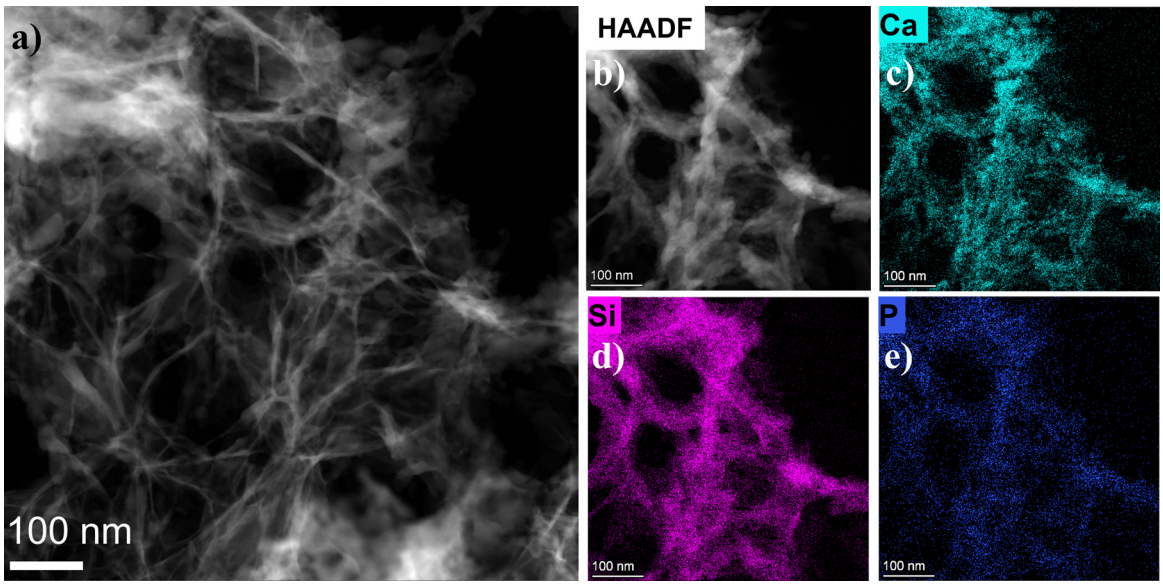

Fig. 7 TEM images of the aliquot after 10 000 s of C–S–H in presence of 100 mg L^{-1} TriP. Shown are (a) the plain TEM image, (b) the HAADF image, and the corresponding EDX-mappings for (c) Ca, (d) Si and (e) P. Scale: 100 nm.

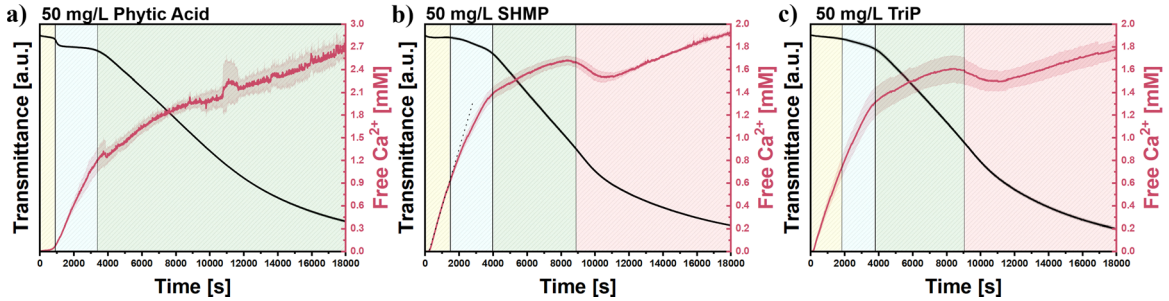

Fig. 8 Crystallization regimes highlighted by *in situ* transmittance and free-Ca^{2+} data for C–A–S–H in the presence of (a) phytic acid, (b) SHMP and (c) TriP, each in a concentration of 50 mg L^{-1}.

cannot be drawn without further investigation. However, the persistent detection of phosphorus by EDX analysis in the 18 000 s samples (Fig. 6) strongly suggests that these phases remain over extended reaction periods.

Collectively, these findings demonstrate that while Ca-phytate formation proceeds *via* rapid, stoichiometric precipitation of solid particles with high phosphate incorporation, SHMP and TriP promote the formation of liquid-like coacervate intermediates through a fundamentally different, phase-separation-driven mechanism. These mechanistic distinctions are reflected not only in the early morphological and compositional signatures captured by TEM, SEM, and EDX, but also in the kinetic profiles revealed by transmittance and free-Ca^{2+} measurements. This validates our methodology as highly effective for distinguishing between different formation mechanisms, demonstrating its broader applicability for systematic comparison of additive effects on cement hydrate formation. The observed differences in Ca–P phase formation pathways, and their subsequent influence on C–S–H nucleation, confirm that P-based additives can modulate cement hydration through mechanisms extending beyond simple calcium complexation.

3.2. Time-resolved analysis of C–A–S–H formation

3.2.1. Transmittance. The C–A–S–H reference sample (black line) demonstrates a distinctive two-step crystallization process, highlighting key differences from C–S–H behaviour as previously documented.[27] While C–S–H systems typically exhibit a nucleation event at approximately 3300 ± 200 s, the C–A–S–H system presents its PoN—marked by the first significant transmittance drop—notably earlier, at around 2800 ± 300 s. This initial transmittance decrease follows a linear trajectory until approximately 7500 ± 300 s, when a pronounced inflection point emerges, marking the transition from linear to exponential decay in transmittance. This point has been identified to a transformation of an initial amorphous C–A–S–H precursor into poorly crystalline C–A–S–H sheets.[27]

When the additives are present, they significantly modify the C–A–S–H precipitation pathway (Fig. 8 and Fig. S5 and S6). Phy (Fig. 8a) induces the characteristic plateau in the transmittance curve, which occurs at similar timepoints and exhibits a comparable magnitude, as observed in C–S–H systems (Fig. S7). This demonstrates clear concentration-dependent behaviour (Fig. 9), suggesting that its calcium interaction

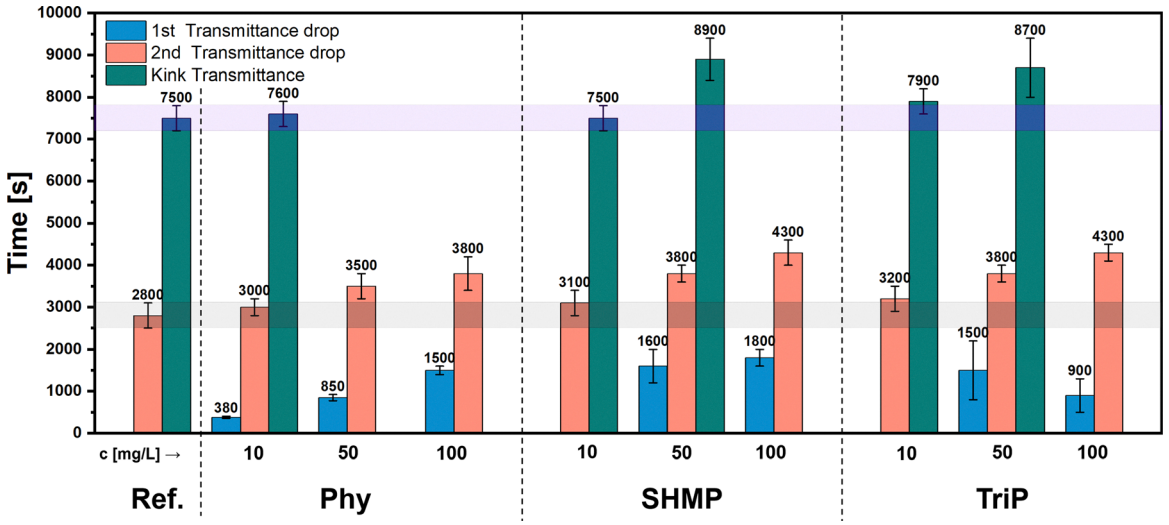

Fig. 9 Durations in the C–A–S–H precipitation titration for each present additive (phytic acid, SHMP, TriP) in various concentrations until the first drop, second drop and kink in the transmittance curve occurred.

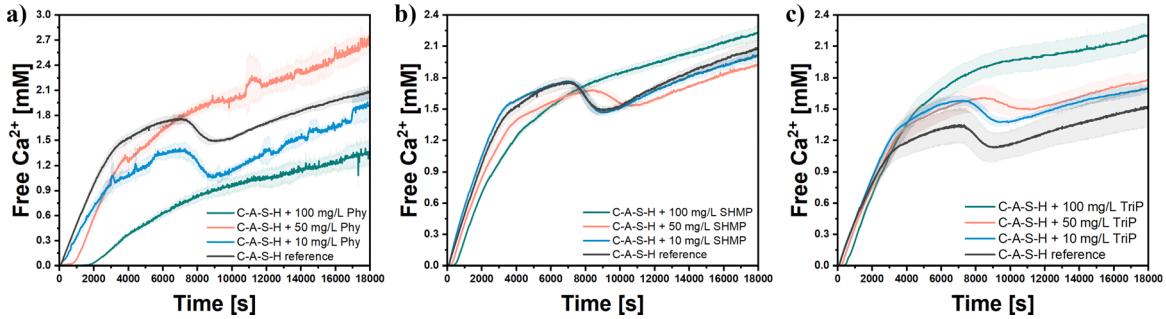

Fig. 10 *In situ* measured free-Ca^{2+} concentration data from the precipitation titrations of C–A–S–H in presence of (a) phytic acid, (b) SHMP and (c) TriP in concentrations of 10, 50 and 100 mg L^{-1}.

operates independently of aluminium presence. Increasing Phy concentration delays the second transmittance decline (corresponding to C–A–S–H precursor formation), though this retardation effect is approximately half than in C–S–H systems.

SHMP (Fig. 8b) and TriP (Fig. 8c) demonstrate also aluminium-mediated effects: their first transmittance drop (Fig. 9) occurs slightly earlier than in C–S–H systems (Fig. 2), indicating that aluminium catalyses the formation of this initial Ca-additive phase, presumably leading to Ca–Al–P coacervate. EDX analysis of 4000 s aliquots (Fig. 6) confirmed aluminium and silicon presence within phosphorus-rich phases (see below). Both SHMP and TriP also retard the second transmittance drop, but their precipitation-inhibiting effect is substantially attenuated in C–A–S–H systems compared to C–S–H systems.

A critical finding across all additives is the concentration-dependent effect on the characteristic transformation kink (C–A–S–H amorphous precursor → C–A–S–H mature). At low concentrations (10 mg L^{-1}), this kink remained clearly observable for all additives, indicating minimal interference with the natural transformation pathway. At intermediate concentrations (50 mg L^{-1}), the response became additive-specific: SHMP and TriP exhibited subtle but detectable transformation signatures, while Phy completely suppressed the kink. At the highest concentration tested (100 mg L^{-1}), all additives consistently eliminated the transformation kink, suggesting either stabilization of the C–A–S–H precursor phase or substantial retardation that would manifest as gradual or imperceptible changes in transmittance, rather than abrupt transitions, consistent with the observed absence of sharp discontinuities in the optical response curves.

3.2.2. Free-Ca^{2+} ion concentration. Distinct regimes can be identified in the free-Ca^{2+} curve in reference C–A–S–H experiments (Fig. 10): an initial linear increase in free Ca^{2+}, followed by a pronounced bending beginning at 3300 ± 300 s and extending for approximately 4000 ± 350 s, a sudden drop in Ca^{2+} concentration at 7300 ± 200 s, and finally a steady increase. These changes correlate directly with transmittance measurements and reflect sequential formation of the C–A–S–H precursor and its subsequent transformation.

Initial calcium binding is similar between C–S–H and C–A–S–H systems (Fig. S8) for the three additives, indicating aluminium species (predominantly $Al(OH)_4^-$ at high pH) do not alter calcium complexation. However, aluminium's presence significantly alters the subsequent phase formation and transformation dynamics. The Ca^{2+} inflection correlating with coacervate formation occurs slightly earlier for SHMP and TriP than in C–S–H systems, confirming aluminium's catalytic role observed in transmittance measurements.

After the formation of Ca–phosphate phases, a notable deviation from the C–A–S–H reference experiment emerges. At 100 mg L^{-1} concentration, all additive-containing experiments show an absence of the characteristic sharp Ca^{2+} maximum, instead exhibiting gradual steady increases. This behaviour confirms the transmittance observations that the sharp two-stage transformation is prevented entirely or significantly retarded, resulting in continuous calcium consumption rather than abrupt precursor conversion. At intermediate concentrations (50 mg L^{-1}), SHMP and TriP exhibit a transitional response where the characteristic Ca^{2+} drops are delayed and prolonged, suggesting that precursor transformation still occurs but at a significantly reduced rate.

3.2.3. C–A–S–H crystallization regimes. Integrated analysis reveals fundamental mechanistic differences between C–A–S–H and C–S–H systems, despite similar initial calcium binding behaviour (Fig. S8).

Looking at the Phy (Fig. 10a) our data suggests that the formation of Ca-phytate phase, which sequesters calcium ions and makes them unavailable for C–A–S–H precursor formation, does indeed delay the formation of the C–A–S–H precursor. However, this delay manifests to a lesser degree than what might be expected from the observed sequestration period (Fig. 8) and markedly reduced relative to the C–S–H system (Fig. S2). This suggests that the formation of the C–A–S–H precursor occurs at substantially lower free-Ca^{2+} concentrations in solution than the reference system (Fig. S3b), indicating that Phy alters the critical supersaturation threshold required for C–A–S–H precursor precipitation.

SHMP (Fig. 10b) and TriP (Fig. 10c) exhibit similar behaviour in C–A–S–H systems as observed in C–S–H, presenting an initial binding regime followed by a linear increase in free Ca^{2+} concentration in solution, both characterized by clear solutions with maximum transmittance. This is followed by a change in slope of the free-Ca^{2+} curve attribute to coacervate formation,

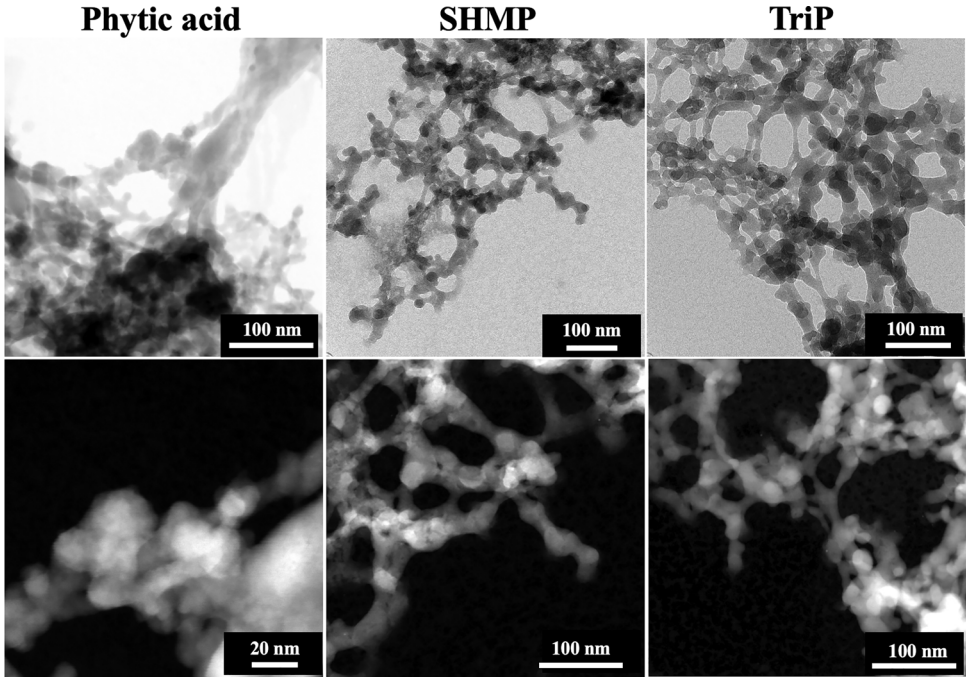

Fig. 11 TEM images of the aliquots taken after 4000 s during the precipitation titration of C–A–S–H in presence of phytic acid, SHMP and TriP in the concentration of 100 mg L^{-1} each.

which causes also the first decrease in transmittance. As mentioned, this transition occurs earlier than in C–S–H systems (Fig. 3b and c), indicating that aluminium has a promoting effect on coacervate formation. Progression through the precipitation pathway shows at 100 mg L^{-1}, all additives converge on similar behaviour—absent transmittance kink and free-Ca^{2+} maxima—indicating precursor stabilization or significantly slowed transformation. Based on analogous stabilization mechanisms observed in amorphous carbonate systems, the observed C–A–S–H precursor stabilization likely occurs through bulk incorporation of phosphate ions within the amorphous matrix, which modifies ion mobility and can alter the crystallization kinetics of metastable amorphous phases,[38] consistent with our observations of eliminated transformation kinks and altered calcium consumption patterns.

3.2.4. Analysis of intermediate phases during C–A–S–H formation. For the C–A–S–H system, we draw aliquots from the media in the 100 mg L^{-1} experiments and investigated them, similarly to the C–S–H system. In this case, only the first aliquot taken at 4000 s was analysed by TEM (Fig. 11) since the amount of sample was low and the second (10 000 s) and final material at 18 000 s were analysed with SEM-EDX since there was enough material.

The precipitates isolated from the Phy system were characterized by network structures containing thicker, seemingly spherical particles. Elemental composition analysis revealed a reduced Ca/Si ratio (1.75 ± 0.35) and low Al/Si ratio (0.68 ± 0.03) compared with the other additives, along with a higher Ca/P ratio (3.76 ± 0.62) already at this timepoint. This compositional profile likely reflects a higher proportion of C–A–S–H phases at this sampling point, as the aliquot was collected shortly before the second transmittance drop occurred. In contrast, the reference C–S–H system still had approximately 1000 s remaining before its second transmittance drop at the equivalent sampling time (Fig. S7).

The SHMP and TriP systems exhibited remarkably similar morphological evolution in C–A–S–H (Fig. 11). The initial aliquot collected at 4000 s revealed a branched nanostructure characterized by significant interconnected porosity, mirroring the C–S–H system and confirming the formation of analogous coacervate phases. TEM images revealed electron-dense nodules (10–30 nm in diameter) interconnected by more electron-transparent bridging regions, creating a continuous three-dimensional network. Compositionally, the SHMP-4000 s samples exhibited a Ca/P molar ratio of 1.70 ± 0.20, while TriP samples showed a ratio of 2.35 ± 0.15 (Fig. 6). Notably, both aluminium and silicon were detected in the isolated coacervate samples, indicating multi-element incorporation during phase formation. EDX local elemental mapping performed during TEM analysis revealed homogeneous distribution of all elements throughout the network structure (Fig. S9), providing evidence for Si and Al incorporation within the coacervate phases formed by both additives. Interestingly, the Al/Si ratio exceeded unity (Fig. S10), suggesting a preferential incorporation of aluminium over silicon within the coacervate matrix. This selective enrichment is particularly noteworthy given that aluminium and silicon were continuously added to the solution at a molar ratio of Al/Si = 0.25. The observed solid-phase Al/Si ratio (>1) represents a four-fold enrichment compared to the solution composition, indicating that the coacervate formation process exhibits strong selectivity for aluminium species over silicate species during phase separation. At these high pH

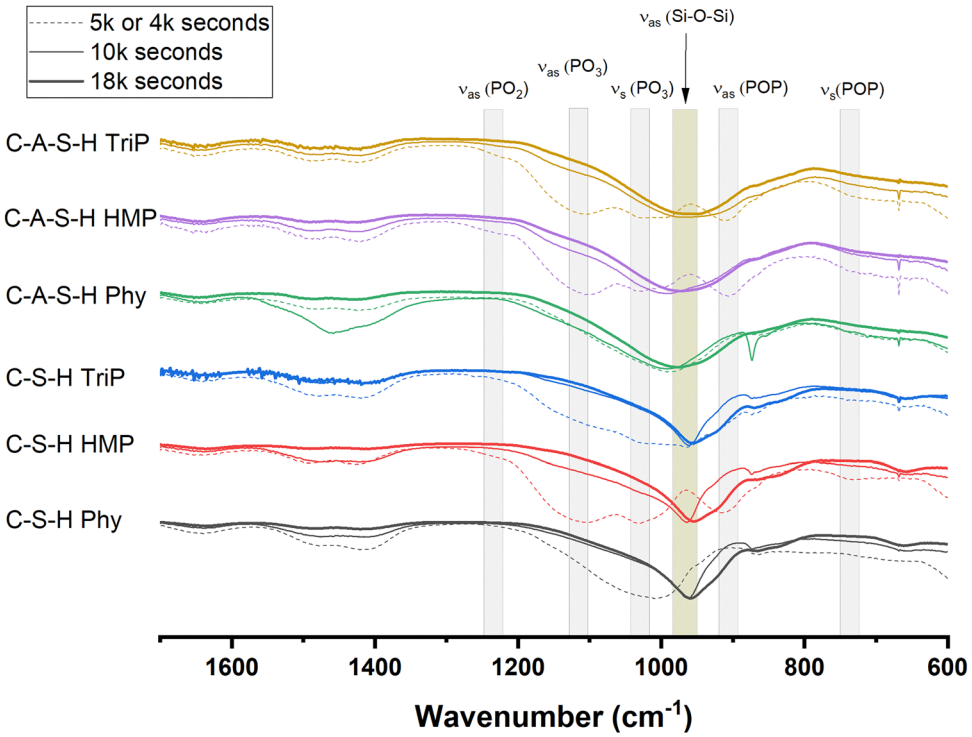

Fig. 12 FTIR spectra of the obtained solids of the aliquots after 4000 & 5000 s (dotted lines), 10 000 s (thin line) and 18 000 s (thick line) during the C–A–S–H synthesis in presence of phytic acid, SHMP and TriP in a concentration of 100 mg L^{-1}.

values, the dominant aluminium species would be the negatively charged aluminate ion ($Al(OH)^{4-}$), which would not directly interact with the negatively charged phosphate groups but instead with the positively charged calcium ions (Ca^{2+}). Ongoing studies in our group are focused on developing improved isolation procedures and implementing shorter time-scale analyses to better characterize all Ca–P phases and its evolutionary pathway.

At 18 000 s, all precipitates approached compositional values similar to the reference C–S–H (Ca/Si = 0.86 ± 0.04, Al/Si = 0.25 ± 0.02), though both ratios remained slightly elevated across all three additive systems (Fig. 6 and Fig. S10). These persistently higher values likely reflect the continued presence of Ca–phosphate coacervate phases and/or residual C–A–S–H precursors, which are characterized by elevated Al/Si ratios compared to mature C–S–H.

3.3. Structural evolution in C–S–H and C–A–S–H systems

3.3.1. FTIR. The FTIR spectra of the reference C–S–H and C–A–S–H phases (Fig. S11) exhibit characteristic peak at around 957 cm^{-1} and 962 cm^{-1}, respectively, attributed to antisymmetric Si–O stretching vibrations of Q^2 tetrahedral units. The absence of a peak at approximately 810 cm^{-1} indicates that no Q^1 units are present in these samples. At 660 cm^{-1}, symmetric bending vibrations of the Si–O–Si bond are visible, while the peak at 1642 cm^{-1} can be assigned to H–O–H bending vibrations of water molecules. The peak at 1415 cm^{-1} relates to slight carbonation. Distinguishing phosphate-related bands in the FTIR spectra proved particularly challenging due to their significant overlap with the main silicate band in both C–S–H and C–A–S–H systems. Despite these spectral limitations, we observed distinct changes in the precipitates collected at different reaction times from experiments with 100 mg L^{-1} concentration (Fig. 12), which revealed a clear temporal evolution of phases in both systems with the additives.

At early reaction times (4000–5000 s), the spectra exhibit characteristic features of calcium–phosphate phases: a broad absorption band centered around 1000 cm^{-1} for Phy, and three defined peaks for SHMP and TriP located at approximately 1115, 1025, and 905 cm^{-1}, with a subtle peak around 730 cm^{-1}. These peaks, assignable to P–O vibrations (Fig. 12), confirm that calcium-additive phases predominate at early reaction stages.

The characteristic Si–O stretching vibration band becomes prominent at intermediate reaction times (10 000 s) signalling the substantial formation of C–S–H or C–A–S–H phases alongside the initial calcium–phosphate precipitates. The central peak of this band appears at significantly higher wavenumbers than typically observed in mature systems, suggesting the presence of more polymerized silicate networks, probably with a higher proportion of Q^3 units compared to mature C–S–H and C–A–S–H hydrates.

As the reaction progresses from 10 000 s to 18 000 s, this band undergoes two significant changes: narrows and transitions to lower wavenumbers. This shift between the 10 000 s and 18 000 s is most pronounced with SHMP additive, reaching around 10 cm^{-1} in C–S–H systems and around 20 cm^{-1} in C–A–S–H systems. The concurrent narrowing and wavenumber

reduction is most likely due to a structural transformation from initially formed metastable silicate(aluminate) networks with higher crosslinked configurations toward precipitates dominated by Q^2 units, characteristic of mature C–S–H or C–A–S–H phases. This observation aligns with prior reports of metastable C–S–H exhibiting a higher proportion of cross-linking sites.[39,40]

Concentration-dependent analysis of samples after 18 000 s revealed that additive concentrations of 10–100 mg L^{-1} produced distinctly different effects on the two cement phases compared to their respective references (Fig. S11). The C–S–H phase exhibited minimal structural changes across all additive concentrations, as evidenced by negligible shifts in characteristic spectral peaks (Fig. S12a) and minimal peak broadening (Fig. S12b), indicating that the additives exerted little perturbation on the silicate framework.

In contrast, the C–A–S–H system displayed systematic shifts to higher wavenumbers in the presence of additives, with particularly pronounced changes (up to 10 cm^{-1}) observed for SHMP and Phy at 100 mg L^{-1} concentrations (Fig. S12a). Peak broadening analysis confirmed this differential response, with higher additive concentrations inducing increased FWHM values (Fig. S12b), further demonstrating the more pronounced effect of additives on the C–A–S–H system. These observations suggest that the additives exert a sustained influence on the aluminosilicate network architecture, preserving elevated concentrations of Q^3 units while impeding their transformation into Q^2-dominated chains. This behaviour correlates with increased Al/Si ratios in these samples, likely reflecting the retention of amorphous C–A–S–H precursor material characterized by higher degrees of polymerization (Fig. S13) and elevated Al/Si ratios (Fig. S10).

The preservation of the C–A–S–H polymerized structure could offer significant advantages for cement performance. Recent work has highlighted the disorder or amorphicity of cement reaction products as an overlooked factor that can enable scientifically guided strategies to design novel cement.[41] The retained Q^3-rich networks observed in our phosphate-modified C–A–S–H systems may contribute to improved binding performance and reduced brittleness, potentially supporting the development of low-carbon cements that achieve enhanced performance with reduced material consumption. On the other side, the stabilization of metastable amorphous phases also raises concerns about potential long-term instability, as delayed phase transformations could compromise matrix integrity over time, highlighting the need for further investigation into these complex stability mechanisms.

3.3.2. XRD. XRD measurements were conducted to investigate the effects of phosphate-containing additives on the crystallinity of the final precipitates. The diffractograms, normalized to the highest peak (29.5°), are shown in Fig. S14 for C–S–H and C–A–S–H, respectively.

The C–S–H reference sample exhibits, as previously described by Kanchanason *et al.*, typical C–S–H reflections at

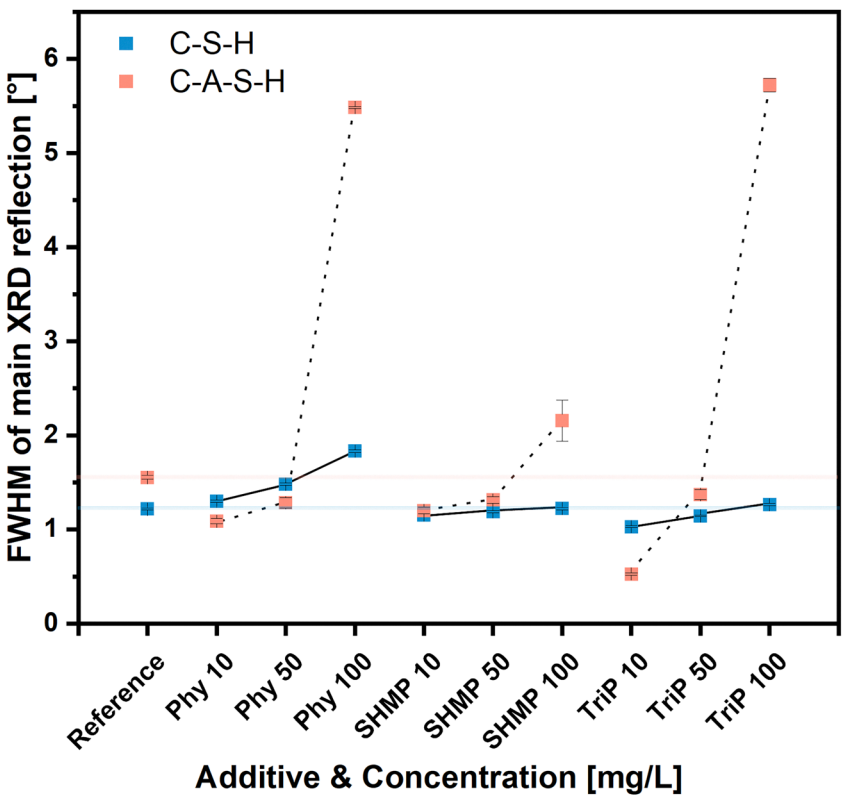

Fig. 13 The measured FWHM from the main reflection of the XRD of the obtained solids from the synthesis of C–S–H and C–A–S–H in presence of phytic acid, SHMP and TriP in concentrations of 10, 50 and 100 mg L^{-1}.

$2\theta = 7.1^\circ$ (d = 12.5 Å), a main reflection at 29.5° (3.1 nm), and a minor shoulder at 32.2° (2.8 nm).[42] This C–S–H pattern derives from tobermorite-like structures affected by nanocrystallinity and turbostratic disorder.[43,44] The XRD pattern shows no evidence of $Ca(OH)_2$ formation.

The reflection at 7.1°, representing the basal spacing of the layered silicate structure, exhibits distinct responses to each phosphate additive. Phy progressively weakens this reflection at 50 mg L^{-1} and eliminates it at 100 mg L^{-1} (Fig. S14a). In contrast, SHMP enhances the reflection's intensity at 50 mg L^{-1}, indicating promotion of the layered structure, with the reflection maintaining its presence across all tested concentrations (Fig. S14b). TriP demonstrates the most significant impact, eliminating the basal spacing reflection at concentrations of 50 mg L^{-1} and above (Fig. S14c). The FWHM values showed that Phy concentration induces a concentration-dependent peak broadening (Fig. 13). In contrast, neither TriP nor SHMP, significantly affected the crystallinity of the C–S–H precipitates. The broadening of the (110) reflection observed with Phy suggests decreased crystallinity. Manifested through smaller crystallite sizes and/or increased lattice distortions and structural disorder. It should be noted, however, that this broadening effect is considerably less pronounced than that observed in C–A–S–H samples, indicating that while Phy influences crystallinity, the structural disruption remains relatively modest.

Concerning the C–A–S–H precipitates, other phases like katoite[45] ($Ca_3Al_2(SiO_4)_3$-$Ca_3Al_2(OH)_{12}$), or strätlingite[46] ($Ca_4Al_2(OH)_{12}$-$[AlSi(OH)_8]_2{\cdot}2H_2O$) were not detected in our XRD patterns. The additives significantly influenced the degree of crystallinity in the C–A–S–H system compared to C–S–H (Fig. S14d–f), as evidenced by changes in the FWHM of the central reflection (Fig. 13). Lower concentrations of the additives (10 mg L^{-1} and 50 mg L^{-1}), seem to not make a big impact on the crystallinity of C–A–S–H compared to the C–A–S–H reference. However, at 100 mg L^{-1} additive concentration, the FWHM increased drastically, indicating the formation of highly amorphous material. This increased amorphicity, reflected in the

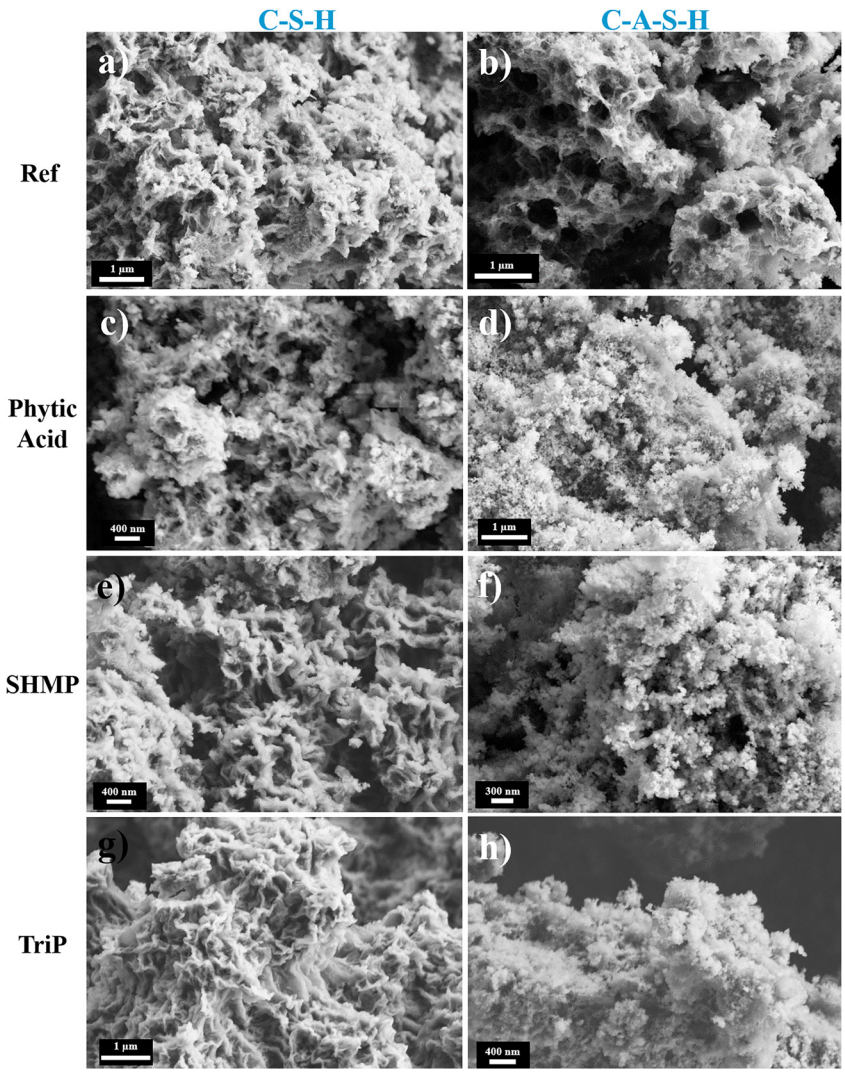

Fig. 14 SEM images of the dried solids from the C–S–H and C–A–S–H precipitation titration in presence of phytic acid, SHMP and TriP in a concentration of 100 mg L^{-1}.

broadening of the 29.5° peak, correlated with shifts to higher wavenumbers in the FTIR spectrum (Fig. S12a) and corresponding spectral broadening (Fig. S12b), confirming the higher presence of C–A–S–H precursor.

3.3.3. Morphological changes introduced by the additives. SEM was used to examine the resulting morphologies of the precipitated C–S–H and C–A–S–H structures after 18 000 s with different concentrations of additives.

The C–S–H reference exhibits a coral-like and porous superstructure (Fig. 14a), which comprises the foils as described in the literature.[42,47] The presence of additives had no discernible influence on the final morphology of the material, regardless of additive type—whether Phy (Fig. 14c and Fig. S15), SHMP (Fig. 14e and Fig. S16), or triP (Fig. 14g and Fig. S17)—or concentration. Despite the likely presence of residual Ca–P phases, the Ca/Si ratios remained relatively consistent across all additive-containing samples (Fig. 6), indicating minimal compositional perturbation of the dominant C–S–H phase.

The C–A–S–H reference displays thinner structures and more porous interweaving than C–S–H (Fig. 14b). In the absence of additives, C–A–S–H undergoes evolution from initial globular precipitates to mature sheet-like structures.[27] However, all three phosphate additives disrupt this natural progression in a concentration-dependent manner. At low concentrations (10 mg L^{-1}), all additives appear to permit normal structural development, allowing C–A–S–H to maintain its morphology with characteristic thin, sheet-like formations (Fig. S15–S17). Conversely, higher concentrations of these additives appear to promote the formation of globular structures (Fig. 14d, f and h). At the highest concentration, this inhibition of morphological transformation generally aligns with the FTIR peaks at higher wavenumbers and the broadening of the 29.6° reflection in XRD, which suggests a greater presence of C–A–S–H precursor at 100 mg L^{-1}. At intermediate concentrations (50 mg L^{-1}), globular structures were also observed; however, FTIR and XRD data indicated reduced polymerization compared to the C–A–S–H precursor. These findings suggest that while the structures preserved the morphological characteristics of their precursors, they exhibited structural tendencies toward the mature C–A–S–H phase. The absence of a defined kink in the transmittance curve supports this interpretation, indicating that the structural transformation occurs gradually rather than through a distinct phase transition.

4. Conclusion & implications

This study offers comprehensive insights into how model phosphate molecules with distinct structures (phytic acid, hexametaphosphate, and tripolyphosphate) impact the formation pathways and final properties of C–S–H and C–A–S–H cement hydrates. Our findings reveal several key mechanisms:

1. Calcium sequestration. Phosphate additives exhibit distinct calcium-binding capacities: Phy shows superior efficiency (Ca/P $\approx$ 0.97) compared to SHMP (Ca/P $\approx$ 0.20) and TriP (Ca/P $\approx$ 0.27). These differences most likely stem from their molecular structures and charge distribution—Phy's inositol ring with R–O–PO_3^{2-} groups carries greater negative charge density with two negative charges per phosphate group, enabling stronger electrostatic interactions with Ca^{2+} ions. Additionally, Phy maintains structural stability in alkaline environments. SHMP's cyclic and TriP's linear configurations, with only one negative charge per phosphate group, undergo hydroxide-induced hydrolysis, compromising their calcium-binding capacity. Aluminium does not seem to influence the Ca-binding.

2. Formation of Ca–phosphate phases. Both C–S–H and C–A–S–H systems exhibit a two-step formation process in the presence of phosphate additives, beginning with distinct Ca-additive phases that influence the subsequent crystallization of C–S–H and C–A–S–H. These intermediate phases differ significantly based on the phosphate type: Phy forms discrete, globular Ca-phytate particles, whereas SHMP and TriP produce interconnected networks consistent with calcium–phosphate coacervates formed *via* liquid–liquid phase separation.

3. Aluminium incorporation in Ca–phosphate phases. In C–A–S–H systems, significant aluminium incorporation occurs in the calcium–phosphate coacervate phase, while silicon is incorporated to a lesser extent despite its fivefold higher concentration. This selective aluminium incorporation accelerates initial precipitate formation compared to C–S–H systems. Additionally, aluminium presence substantially reduces the retardation effect of phosphate additives on C–A–S–H hydrate formation.

4. Effect on the final C–S–H precipitates. Phosphate additives do not affect the coral-like structure of C–S–H while causing minor molecular changes. Phy increases structural disorder, whereas SHMP improves organization at moderate concentrations. Phosphorus remains in the final material, indicating that calcium–phosphate phases persist within the C–S–H structure.

5. C–A–S–H precursor stabilization. At higher concentrations (100 mg L^{-1}), the three additives stabilize the early globular C–A–S–H phase, preventing its normal development into sheet-like structures. This results in solids that are more polymerized and less crystalline throughout the reaction, demonstrating the additives' ability to halt C–A–S–H maturation at a more amorphous state.

These findings have important implications for cement hydration control, workability enhancement, and hydrate phase modification:

1. Retardation mechanisms. This study reveals that phosphate additives impede homogeneous hydrate formation through dual mechanisms: direct calcium ion sequestration and formation of stable calcium–phosphate phases. These phases persist rather than dissolve during the early stages of hydrate formation, suggesting potential impacts on material properties. Further investigation is needed to determine their stability in cement pastes and their effects over extended timeframes.

2. Implications for cement workability. The ability of the tested additives to delay C–S–H formation has significant

potential for enhancing cement workability. By delaying the onset of setting, these simple P-additives could provide extended handling times without compromising final strength development, addressing a critical challenge in concrete placement. However, the substantially reduced retardation effects in C–A–S–H systems suggest limited effectiveness in blended cements containing aluminium-rich supplementary cementitious materials, potentially restricting their application in modern sustainable cement formulations.

3. Considerations for Al-Containing SCMs. The extended lifetime of the C–A–S–H precursor phase observed has important implications for blended cements using SCMs containing aluminium. This prolonged stability of the amorphous precursor could influence mechanical properties and durability through multiple pathways. From a sustainable cement design perspective, the enhanced amorphicity may enable improved binding performance and reduced brittleness. However, this could also create risks of delayed phase transformations that might compromise long-term matrix stability. Therefore, caution is required when using additives designed for a single purpose, as they may induce multiple unintended effects. In the case of C–A–S–H systems, while the tested phosphate additives show limited effectiveness as retardants, they could prove valuable for enhancing the cement paste matrix through controlled modification of the hydrate characteristics.

Conflicts of interest

The authors declare that they have no affiliation with any organization with a direct or indirect financial interest in the discussed subject matter of this paper.

Data availability

Data for this article are available at yannick-hermann.emminger@uni-konstanz.de.

Supporting data for this article has also been included in the supplementary information (SI). Supplementary information is available. See DOI: https://doi.org/10.1039/d5ma00758e.

Acknowledgements

Cristina Ruiz Agudo expresses her gratitude to the Zukunftskolleg (University of Konstanz) and 'Dres. Edith and Klaus Dyckerhoff Foundation' for their financial support for this project. This project has received funding from the European Union's Horizon Europe research and innovation programme under grant agreement No 101131765 (EXCITE2) for Transnational Access conducted at the University of Granada, Spain.

References

1 I. Kirchberger, F. Goetz-Neunhoeffer and J. Neubauer, Enhancing the aluminate reaction during OPC hydration by combining increased sulfate content, triethanolamine and tartaric acid, *Cem. Concr. Res.*, 2023, **170**, 107188.
2 N. B. Singh, Effect of gluconates on the hydration of cement, *Cem. Concr. Res.*, 1976, **6**, 455–460.
3 G. Kastiukas, X. Zhou, J. Castro-Gomes, S. Huang and M. Saafi, Effects of lactic and citric acid on early-age engineering properties of Portland/calcium aluminate blended cements, *Constr. Build. Mater.*, 2015, **101**, 389–395.
4 G. Möschner, B. Lothenbach, R. Figi and R. Kretzschmar, Influence of citric acid on the hydration of Portland cement, *Cem. Concr. Res.*, 2009, **39**, 275–282.
5 N. L. Thomas and J. D. Birchall, The retarding action of sugars on cement hydration, *Cem. Concr. Res.*, 1983, **13**, 830–842.
6 L. Zhang, *et al.*, Effects of Saccharide Set Retarders on the Hydration of Ordinary Portland Cement and Pure Tricalcium Silicate, *J. Am. Ceram. Soc.*, 2010, **93**, 279–287.
7 M. Bishop and A. R. Barron, Cement Hydration Inhibition with Sucrose, Tartaric Acid, and Lignosulfonate: Analytical and Spectroscopic Study, *Ind. Eng. Chem. Res.*, 2006, **45**, 7042–7049.
8 D. Axthammer and J. Dengler, Cement retarding mechanism of phosphonates and their interaction with aluminium, *Mater. Adv.*, 2024, **5**, 5974–5983.
9 H. Tan, *et al.*, Effect of the Adsorbing Behavior of Phosphate Retarders on Hydration of Cement Paste, *J. Mater. Civ. Eng.*, 2017, **29**, 04017088.
10 W. Chen, *et al.*, Experimental evidence on formation of ulexite in sulfoaluminate cement paste mixed with high concentration borate solution and its retarding effects, *Constr. Build. Mater.*, 2019, **215**, 777–785.
11 J. F. Young, A review of the mechanisms of set-retardation in portland cement pastes containing organic admixtures, *Cem. Concr. Res.*, 1972, **2**, 415–433.
12 K. G. Fikeni, *et al.*, An overview of oil well cement retarders and the retardation mechanisms, *Geoenergy Sci. Eng.*, 2024, **241**, 213116.
13 H. Sui, *et al.*, Limestone calcined clay cement: mechanical properties, crystallography, and microstructure development, *J. Sustain. Cem.-Based Mater.*, 2023, **12**, 427–440.
14 H. Kim, H. M. Son and H. K. Lee, Review on recent advances in securing the long-term durability of calcium aluminate cement (CAC)-based systems, *Funct. Compos. Struct.*, 2021, **3**, 035002.
15 S. Karthika, T. K. Radhakrishnan and P. Kalaichelvi, A Review of Classical and Nonclassical Nucleation Theories, *Cryst. Growth Des.*, 2016, **16**, 6663–6681.
16 D. Gebauer, M. Kellermeier, J. D. Gale, L. Bergström and H. Cölfen, Pre-nucleation clusters as solute precursors in crystallisation, *Chem. Soc. Rev.*, 2014, **43**, 2348–2371.
17 C. Ruiz-Agudo and H. Cölfen, Exploring the Potential of Nonclassical Crystallization Pathways to Advance Cementitious Materials, *Chem. Rev.*, 2024, **124**, 7538–7618.
18 D. Gebauer, How Can Additives Control the Early Stages of Mineralisation?, *Minerals*, 2018, **8**, 179.

19 K. Hurle, *et al.*, Hydration mechanism of a calcium phosphate cement modified with phytic acid, *Acta Biomater.*, 2018, **80**, 378–389.
20 T. Zhang, L. J. Vandeperre and C. R. Cheeseman, Formation of magnesium silicate hydrate (M-S-H) cement pastes using sodium hexametaphosphate, *Cem. Concr. Res.*, 2014, **65**, 8–14.
21 M. Ltifi, A. Guefrech and P. Mounanga, Effects of sodium tripolyphosphate addition on early-age physico-chemical properties of cement pastes, *Proc. Eng.*, 2011, **10**, 1457–1462.
22 O. Uyanik, *et al.*, Effect of phytic acid on the setting times and tensile strengths of calcium silicate-based cements, *Aust. Endod. J.*, 2019, **45**, 241–245.
23 B. Cheng, *et al.*, Effects of Sodium Hexametaphosphate Addition on the Dispersion and Hydration of Pure Calcium Aluminate Cement, *Materials*, 2020, **13**, 5229.
24 A. Malik, *et al.*, A common food additive (E452), hexametaphosphate, denatures the digestive enzyme trypsin, *J. King Saud Univ. Sci.*, 2023, **35**, 102968.
25 H. Tan, *et al.*, Effect of competitive adsorption between polycarboxylate superplasticiser and sodium tripolyphosphate on cement paste fluidity, *Adv. Cem. Res.*, 2015, **27**, 593–600.
26 B. Cheng, *et al.*, Effects of Sodium Tripolyphosphate Addition on the Dispersion and Hydration of Pure Calcium Aluminate Cement, *Materials*, 2023, **16**, 3141.
27 Y. H. Emminger, L. Ladner and C. Ruiz-Agudo, Comparative study of the early stages of crystallization of calcium silicate hydrate (C-S-H) and calcium aluminate silicate hydrate (C-A-S-H), *Cem. Concr. Res.*, 2025, **193**, 107873.
28 F. Crea, P. Crea, A. De Robertis and S. Sammartano, Speciation of phytate ion in aqueous solution. Characterisation of Ca-phytate sparingly soluble species, *Chem. Speciation Bioavailability*, 2004, **16**, 53–59.
29 T. Dürr-Mayer, *et al.*, Non-Hydrolysable Analogues of Cyclic and Branched Condensed Phosphates: Chemistry and Chemical Proteomics, *Chem. – Eur. J.*, 2023, **29**, e202302400.
30 M. Tonelli, *et al.*, Effect of phosphate additives on the hydration process of magnesium silicate cements: Thermal and spectroscopic characterization, *J. Therm. Anal. Calorim.*, 2019, **138**, 3311–3321.
31 T. E. Robinson, L. A. Arkinstall, S. C. Cox and L. M. Grover, Determining the Structure of Hexametaphosphate by Titration and ^{31}P-NMR Spectroscopy, *Comments Inorg. Chem.*, 2022, **42**, 47–59.
32 J. G. Hamilton, D. Hilger and D. Peak, Mechanisms of tripolyphosphate adsorption and hydrolysis on goethite, *J. Colloid Interface Sci.*, 2017, **491**, 190–198.
33 Y. Song, X. Guo, Y. Bu, Y. Zhang and L. Tian, Hydration and degradation mechanism of sodium hexametaphosphate chemically bonded material under CO2 sequestration, *Geoenergy Sci. Eng.*, 2024, **234**, 212641.
34 M. Cheryan and J. J. Rackis, Phytic acid interactions in food systems, *Crit. Rev. Food Sci. Nutr.*, 1980, **13**, 297–335.
35 W. E. G. Müller, *et al.*, Functional importance of coacervation to convert calcium polyphosphate nanoparticles into the physiologically active state, *Mater. Today Bio*, 2022, **16**, 100404.
36 A. Momeni and M. J. Filiaggi, Comprehensive Study of the Chelation and Coacervation of Alkaline Earth Metals in the Presence of Sodium Polyphosphate Solution, *Langmuir*, 2014, **30**, 5256–5266.
37 J. Soulié, *et al.*, Development of a new family of monolithic calcium (pyro)phosphate glasses by soft chemistry, *Acta Biomater.*, 2016, **41**, 320–327.
38 Z. Zou, *et al.*, Additives Control the Stability of Amorphous Calcium Carbonate via Two Different Mechanisms: Surface Adsorption versus Bulk Incorporation, *Adv. Funct. Mater.*, 2020, **30**, 2000003.
39 J. Plank, M. Schönlein and V. Kanchanason, Study on the early crystallization of calcium silicate hydrate (C-S-H) in the presence of polycarboxylate superplasticizers, *J. Organomet. Chem.*, 2018, **869**, 227–232.
40 X. Shen, *et al.*, New insights into the non-classical nucleation of C-S-H, *Cem. Concr. Res.*, 2023, **168**, 107135.
41 H. Nguyen and P. Kinnunen, What makes cements bind? —A proposal for a universal factor, *Mater. Adv.*, 2024, **5**, 5036–5040.
42 V. Kanchanason and J. Plank, Role of pH on the structure, composition and morphology of C-S-H–PCE nanocomposites and their effect on early strength development of Portland cement, *Cem. Concr. Res.*, 2017, **102**, 90–98.
43 N. Krautwurst, *et al.*, Two-Step Nucleation Process of Calcium Silicate Hydrate, the Nanobrick of Cement, *Chem. Mater.*, 2018, **30**, 2895–2904.
44 S. Grangeon, *et al.*, Structure of nanocrystalline calcium silicate hydrates: insights from X-ray diffraction, synchrotron X-ray absorption and nuclear magnetic resonance, *J. Appl. Crystallogr.*, 2016, **49**, 771–783.
45 E. Passaglia and R. Rinaldi, Katoite, a new member of the $Ca_3Al_2(SiO_4)_3$-$Ca_3Al_2(OH)_{12}$ series and a new nomenclature for the hydrogrossular group of minerals, *Bull. Mineral.*, 1984, **107**, 605–618.
46 I. Santacruz, *et al.*, Structure of stratlingite and effect of hydration methodology on microstructure, *Adv. Cem. Res.*, 2016, **28**, 13–22.
47 M. Schönlein and J. Plank, A TEM study on the very early crystallization of C-S-H in the presence of polycarboxylate superplasticizers: Transformation from initial C-S-H globules to nanofoils, *Cem. Concr. Res.*, 2018, **106**, 33–39.